The Astrophysical Journal, 975:287 (15pp), 2024 November 10 https://doi.org/10.3847/1538-4357/ad7eb6

A New Framework for Understanding Systematic Errors in Cluster Lens Modeling. III. Deflection from Large-Scale Structure

Aniruddha Madhava and Charles R. Keeton

Rutgers University–New Brunswick, Department of Physics and Astronomy, 136 Frelinghuysen Rd., Piscataway, NJ 08854, USA; keeton@rutgers.edu

Received 2024 July 17; revised 2024 September 19; accepted 2024 September 22; published 2024 November 8

Abstract

Interpreting and reconstructing distant sources that are gravitationally lensed by galaxy clusters requires accurate and precise lens models. While high-quality data sets have reduced statistical errors in such models, systematic errors remain important. We examine systematic lensing effects caused by density fluctuations due to large-scale structure along the line of sight. We use a multiplane ray-tracing algorithm with the IllustrisTNG 100-3 cosmological simulation of matter distribution and compute the statistical distributions of shear, convergence, and higher-order deflections using two Hubble Frontier Field clusters as examples (A2744 and MACS J0416.1−2403). The cosmic shear distribution is Gaussian in each component, while the cosmic convergence distribution is skewed such that $1+\kappa$ is consistent with a log-normal distribution; the standard deviations for these quantities are at the level of a few to 10%, depending on the redshift of the source. The deflection from higher-order terms beyond convergence and shear has significant scatter: the rms deflection is $\sim 15''$, considerably larger than the image position residuals for current lens models. These results indicate that line-of-sight deflection effects due to large-scale structure can significantly impact lens models and should not be neglected. We present results in forms that can be incorporated into future cluster lens models.

Unified Astronomy Thesaurus concepts: Gravitational lensing (670); Galaxy clusters (584); Abell clusters (9)

1. Introduction

With masses of 10^{14}–$10^{15}\,M_\odot$, galaxy clusters act as powerful gravitational lenses to magnify distant galaxies (e.g., S. Kikuchihara et al. 2020) and offer a variety of astrophysical applications. For instance, B. L. Frye et al. (2023) and the JWST `PEARLS` team report more diversity than expected among galaxies magnified by the El Gordo cluster (ACT-CL J0102−4915). L. J. Furtak et al. (2021) analyze the robustness of constraints on the low mass end of the $z\sim 6$–7 stellar mass function using Hubble Frontier Fields (HFF) lensing observations (J. M. Lotz et al. 2017).

To study the galaxies lensed by clusters, it is necessary to account for lensing distortion and magnification using lens models that capture the complexity of the cluster and its environment in some appropriate level of detail (e.g., J.-P. Kneib & P. Natarajan 2011). The amount of high-quality data has significantly improved in recent years, and cluster lens models have become increasingly sophisticated. C. A. Raney et al. (2020b) compared models of the HFF clusters from different modeling teams and found that statistical uncertainties have decreased, but there are still systematic effects that are important to understand. Our group has begun examining different modeling choices to see how much they contribute to the systematic uncertainties. For example, C. A. Raney et al. (2020a) considered the effects of including galaxies along the line of sight (LOS). C. A. Raney et al. (2021, Paper I in this series) analyzed the selection and treatment of cluster member galaxies, and D. T. Zimmerman et al. (2021, Paper II) studied the choice of lensed images used as constraints.

One factor that should be explored further is deflection by large-scale structure along the LOS. In standard lens models, the mass density is assumed to equal the mean density of the Universe everywhere except in the main lens plane. Under this assumption, lensing deflection occurs only at the cluster redshift. However, density fluctuations due to large-scale structure can create additional deflections that might not be negligible given the precision of current lens data and models.

In principle, one could try to model the entire LOS for an observed lens system and explicitly include it in lens models (e.g., C. McCully et al. 2017). However, this approach requires extensive photometric and spectroscopic observations to characterize all of the galaxies along the LOS, along with strong assumptions about how the observed galaxies trace the underlying mass distribution; so it is costly and introduces new types of systematic uncertainties. An alternative approach is to estimate deflections from large-scale structure using theory and/or simulations. R. Bar-Kana (1996), O. Host (2012), and A. D'Aloisio et al. (2014) used the power spectrum of density fluctuations to compute cosmic convergence and shear (which are the lowest-order terms in a Taylor series expansion of the deflection). S. Hilbert et al. (2009) instead used ray tracing through the Millennium Simulation (V. Springel et al. 2005), which better captures higher-order effects in both the density distribution and the light bending. Here, we adopt a similar ray-tracing analysis, apply it to the IllustrisTNG simulations (R. Weinberger et al. 2017; F. Marinacci et al. 2018; J. P. Naiman et al. 2018; D. Nelson et al. 2018; A. Pillepich et al. 2018b, 2018a; V. Springel et al. 2018), and quantify the results in a form needed for the cluster lens modeling framework introduced by C. A. Raney et al. (2021). Section 2 summarizes the various components of our methodology, Section 3 presents our results, and Section 4 summarizes conclusions and implications for future work.

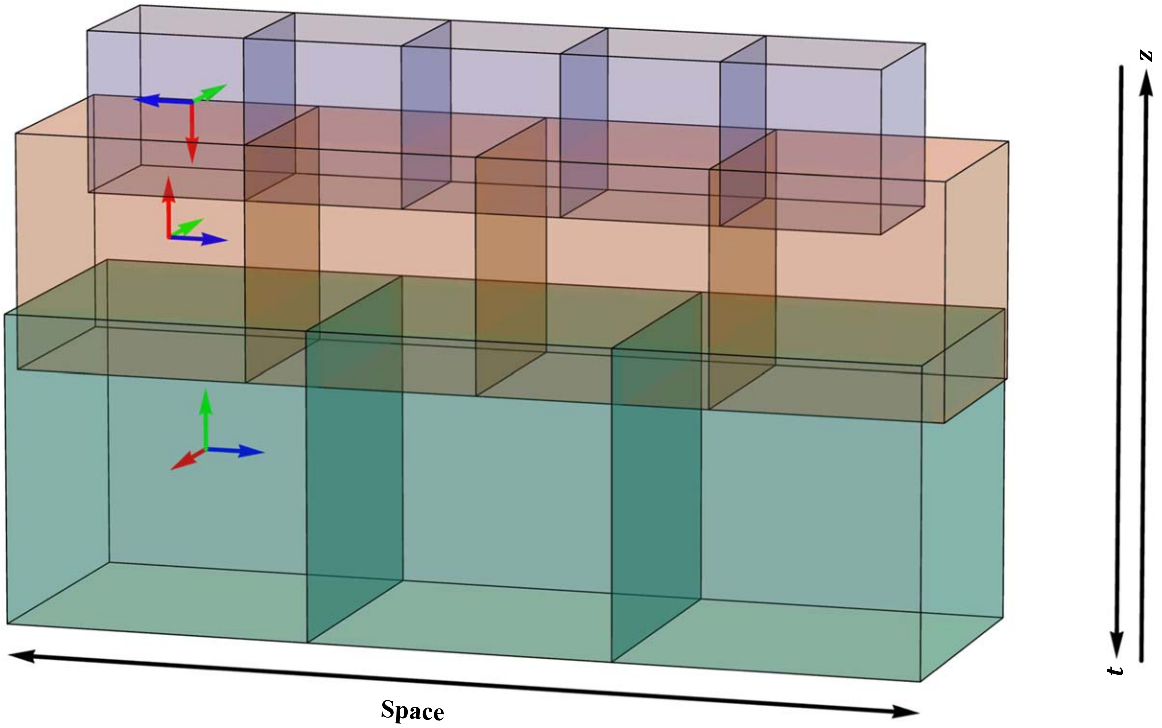

Figure 1. Schematic representation of how we use simulation boxes to fill the volume. Boxes of the same color correspond to a given snapshot; they can be tiled in the spatial directions thanks to periodic boundary conditions. To prevent light rays from repeatedly traversing the same region, we apply random rotations to each snapshot box (depicted by the coordinate axes: X-axis in red, Y-axis in blue, and Z-axis in green), as well as random spatial translations between consecutive snapshots. Given the simulation size and distance between slices, boxes may overlap and we must take care not to double count mass in the overlap regions (see Figure 2 for details). Note: in this figure, time flows from top to bottom, so redshift increases from bottom to top.

2. Methodology

2.1. Simulations

The IllustrisTNG Project is a family of 18 magnetohydrodynamical simulations of galaxy formation that explicitly treat different types of "particles" including dark matter, gas, and stars in a cosmological context (R. Weinberger et al. 2017; F. Marinacci et al. 2018; J. P. Naiman et al. 2018; D. Nelson et al. 2018; A. Pillepich et al. 2018b, 2018a; V. Springel et al. 2018). The three primary simulation series are `TNG50`, `TNG100`, and `TNG300`, which have box sizes of 51.7, 110.7, and 302.6 comoving megaparsecs (cMpc), respectively. All of the simulations use periodic boundary conditions and Planck 2015 cosmological parameters: energy density $\Omega_\Lambda = 0.6911$, matter density $\Omega_m = 0.3089$, and Hubble parameter $h = 0.6774$ (Planck Collaboration et al. 2016). More information about the simulations can be found in the IllustrisTNG data release papers and website.[1]

For our purposes, the `TNG100-3` simulation (the third run in the `TNG100` family) provides a good balance between the size of the simulation and the volume of data. The simulation box is large enough to allow ~5000 independent samples of the image configurations at the highest redshifts we consider, and even more at lower redshifts (see Figures 3 and 4 below), while the smoothing length (0.74 comoving kpc) is considerably smaller than the separation between lensed images. (The `TNG300` family of simulations offers larger simulation boxes, but the smoothing length is closer to the typical image separations.) The public data set includes 100 snapshots ranging from redshift 20.05 to 0. The main contributions to lensing typically occur at redshifts $z \lesssim 1$, so we consider the snapshots from 50 ($z = 1.00$) to 98 ($z = 0.01$).

Figure 1 illustrates how we use simulation boxes. For each snapshot, we can use periodic boundary conditions to tile the spatial directions; then, we can combine the different snapshots to fill the volume between the observer and sources. There are two important details. First, in the simplest construction, a light ray may repeatedly encounter the same structure at different epochs of formation. S. Hilbert et al. (2009) address this issue by carefully choosing angles for light rays to minimize the number of repetitions. We take a different approach: we rotate each snapshot box so we are viewing a random face with a random orientation, and we apply a random spatial translation between consecutive snapshots. These effects, which are depicted in Figure 1, combine to provide a reliable statistical sampling of large-scale structure.

The second detail is that simulation boxes may overlap along the LOS. If this issue is not addressed, we could overcount mass in the overlap regions. S. Hilbert et al. (2009) resolve this problem by grouping halos into the snapshot slice that contains their centers, and giving special attention to halos that may move across slice boundaries between snapshots. Since we operate on individual particles instead of halos, we simply place bounds on the range of Z coordinates used in each snapshot box, as depicted at the top of Figure 2.

2.2. Lensing Framework

We follow the lensing framework introduced by C. A. Raney et al. (2021) and review the key points here.

---

[1] https://www.tng-project.org/data/

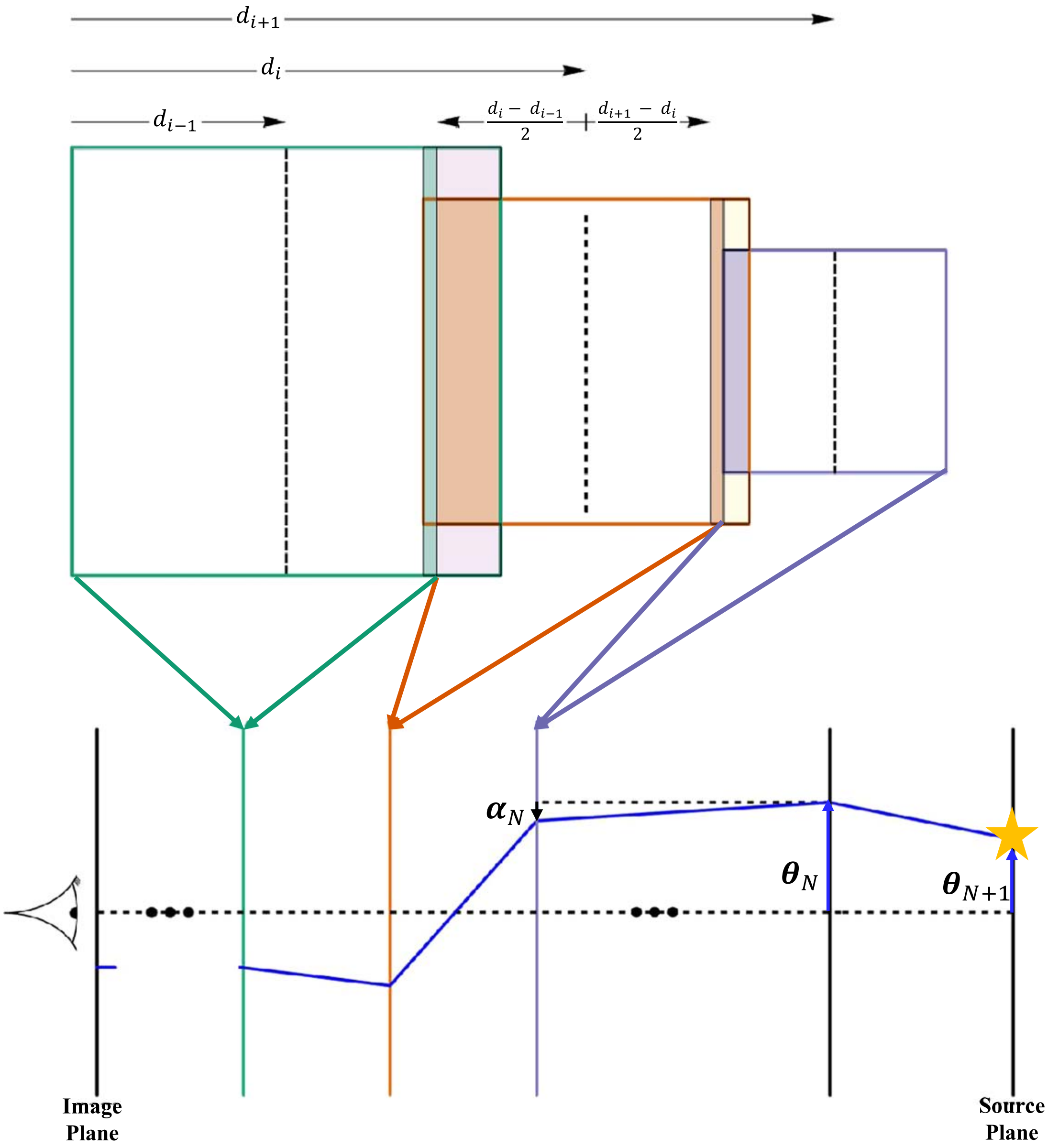

Figure 2. Top: d_{i-1}, d_i, d_{i+1} are the angular diameter distances to three sample simulation boxes. Indices increase from left to right, consistent with lensing conventions in Equation (1). Simulation boxes whose snapshots are close in redshift may overlap. To avoid double-counting these regions, we implement upper and lower bounds for particle redshift for each box. Mass in the green region is allocated to plane $i-1$; mass in the orange regions is allocated to i, and mass in the dark purple region is allocated to plane $i+1$. Mass in the light purple and yellow regions are overlaps between box i and copies of $i-1$ and $i+1$ (due to periodic boundary conditions). Hence, these regions are not allocated to any plane. Bottom: simulations boxes are projected into planes and combined using the multiplane lens equation. Time flows from right to left, while redshift increases from left to right.

2.2.1. Lens Equation

Each simulation snapshot is projected to obtain a surface mass density, and the different snapshots are combined using the multiplane lens equation (e.g., P. Schneider et al. 1992; A. O. Petters et al. 2001; C. McCully et al. 2014). Consider N lens planes with index i that increase away from the observer. Let $\boldsymbol{\theta}_i$ be the angular position of the light ray in plane i, and $\boldsymbol{\alpha}_i$ be the bending angle created by the mass in that plane. The lens equation can be obtained from the recursive ray-tracing equation:

$$\boldsymbol{\theta}_j = \boldsymbol{\theta}_1 - \sum_{i=1}^{j-1} \frac{D_{ij}}{D_j} \boldsymbol{\alpha}_i(\boldsymbol{\theta}_i), \tag{1}$$

where D_i is the angular diameter distance to plane i, and D_{ij} is the angular diameter distance from plane i to plane j. The source plane can be treated as plane $N+1$. Equation (1) is computationally inefficient because each plane involves a sum over all foreground planes, so the total number of terms is of order $N(N-1)/2$. S. Hilbert et al. (2009) present an equivalent formulation in which plane $j+1$ can be computed in terms of planes j and $j-1$:

$$\boldsymbol{\theta}_{j+1} = \boldsymbol{\theta}_j + \varepsilon_j(\boldsymbol{\theta}_j - \boldsymbol{\theta}_{j-1}) - \frac{D_{j,j+1}}{D_{j+1}} \boldsymbol{\alpha}_j(\boldsymbol{\theta}_j), \tag{2}$$

where

$$\varepsilon_j = \frac{D_j D_{j-1,j+1}}{D_{j-1,j} D_{j+1}} - 1. \tag{3}$$

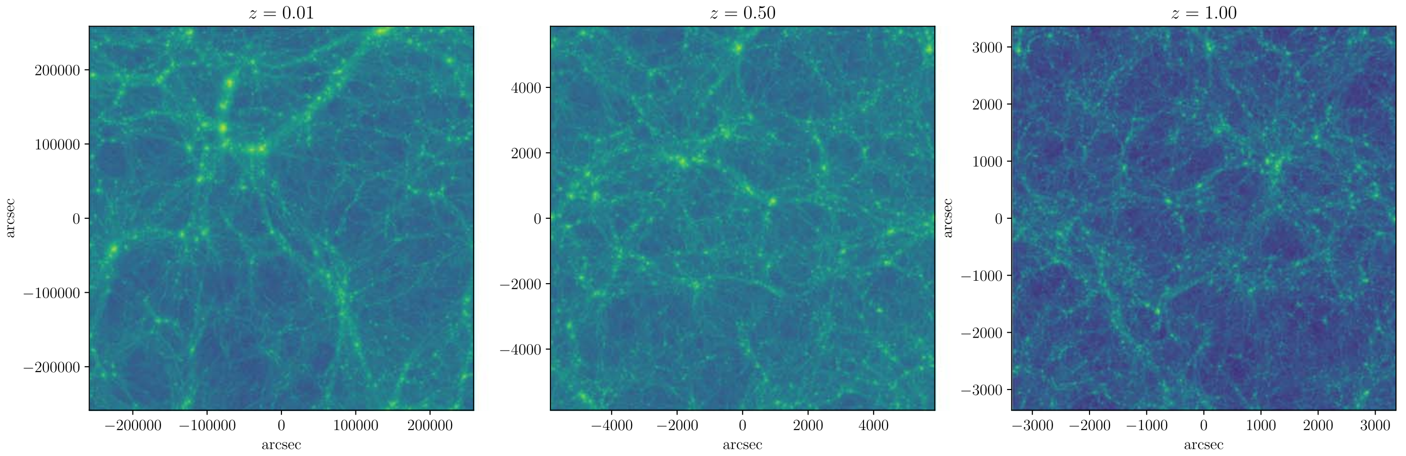

Figure 3. Examples of surface mass density maps for three snapshots of the `TNG100-3` simulation. The density maps have the same comoving dimension (110.7 cMpc) but different angular scales.

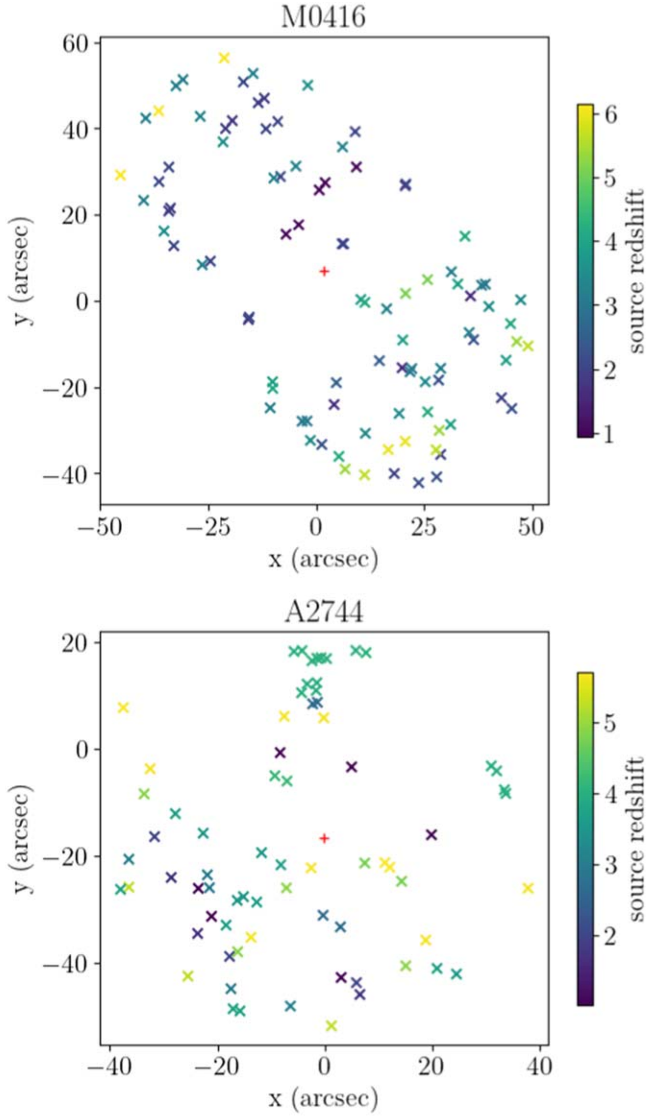

Figure 4. Image configurations for two of the Hubble Frontier Fields clusters: MACS J0416−1.2023 (top) and A2744 (bottom). Colored × indicate observed images, with points color-coded by the redshift of the source. Red + indicates the reference position (assumed to have source redshift $z_s = 2.0$).

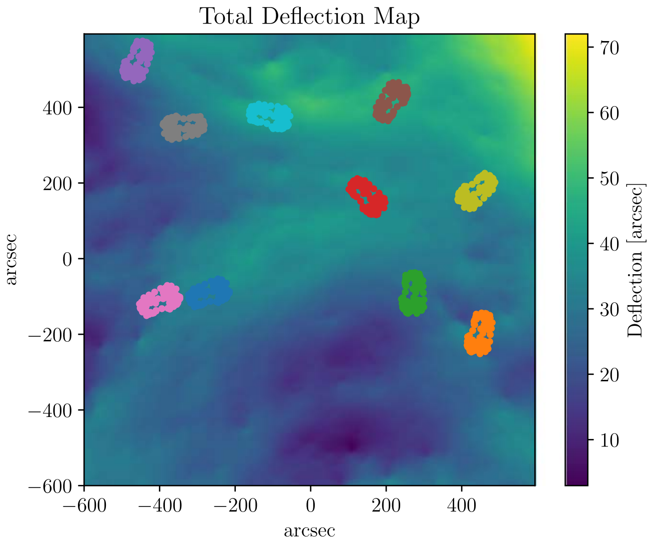

Figure 5. Illustration of our process of translating and rotating an image configuration (M0416 is used here) to compute deflection statistics. Here, multiple realizations are shown on a single deflection map. However, in our full analysis, each realization has a random shift applied to each lens plane (see Section 2.1) to produce a new total deflection map.

Note that both versions of the lens equation involve distance ratios, so it is equivalent to use angular diameter distances or transverse comoving distances as the ratios are the same in either case. See the bottom part of Figure 2 for a depiction of the multiplane lens equation.

For cluster lensing, it makes sense to distinguish the plane that contains the cluster from the remaining large-scale structure planes. C. A. Raney et al. (2021) do this by writing the lens equation in the form

$$\boldsymbol{\beta} = \boldsymbol{\theta} - \boldsymbol{\alpha}_{\rm clus}(\boldsymbol{\theta} - \boldsymbol{\alpha}_{\rm fg}(\boldsymbol{\theta})) - \boldsymbol{\alpha}_{\rm los}(\boldsymbol{\theta}), \tag{4}$$

where $\boldsymbol{\theta}$ is the image position and $\boldsymbol{\beta}$ is the source position. Here, $\boldsymbol{\alpha}_{\rm clus}$ is the deflection produced by the cluster, while $\boldsymbol{\alpha}_{\rm los}$ is the deflection produced by the rest of the mass along the LOS, while $\boldsymbol{\alpha}_{\rm fg}$ is the deflection produced by mass in the

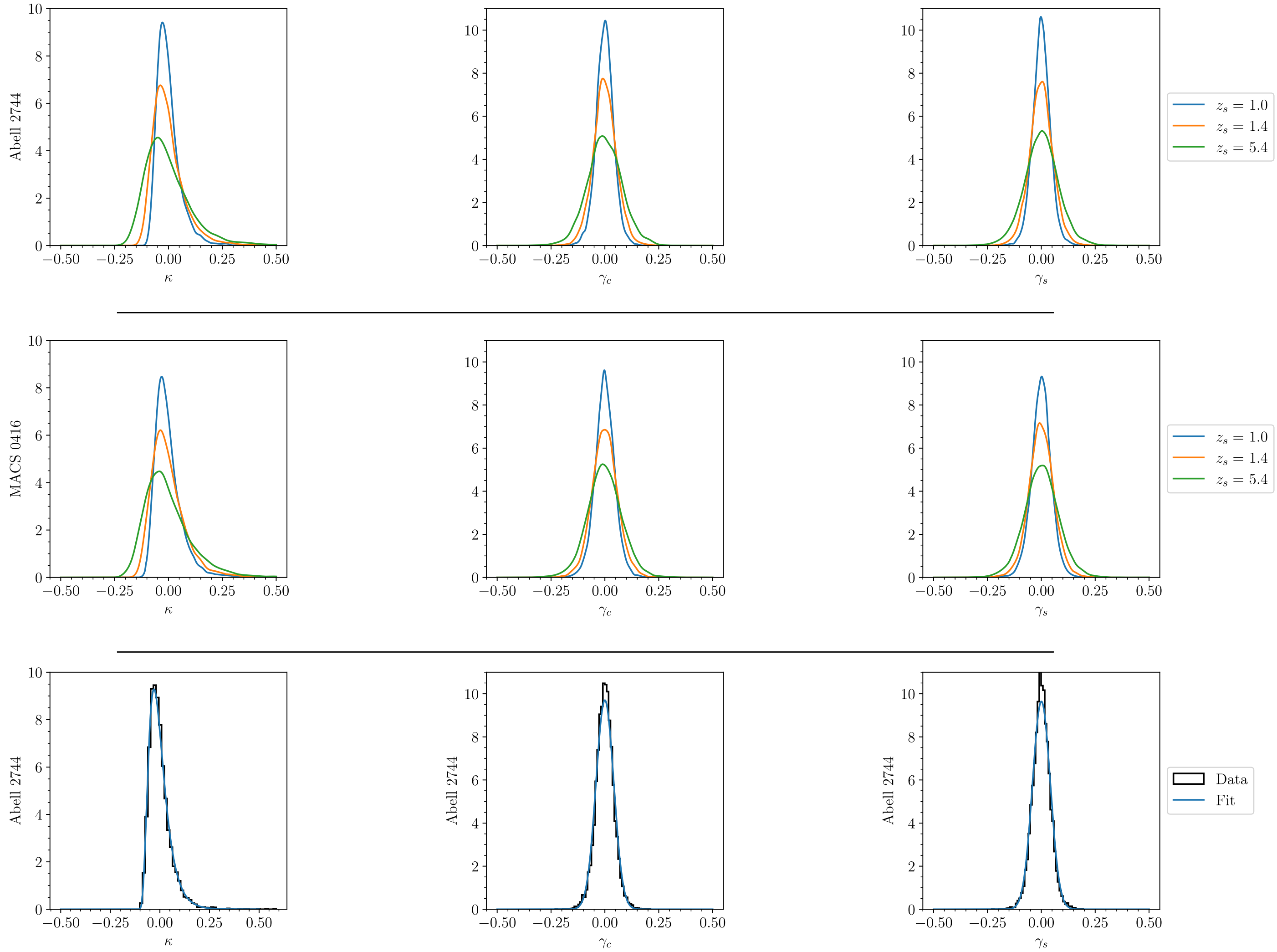

Figure 6. Distributions of cosmic convergence and shear computed using the two cluster image configurations (top two rows), for three sample redshifts chosen to illustrate how the distributions evolve. The curves shown here are computed from the 10,000 realizations using Gaussian kernel density estimation (KDE). The bottom row directly compares the KDE fits (smooth curves) with the sample histograms for A2744.

foreground (between the observer and the cluster). The latter two quantities can be written as

$$\boldsymbol{\alpha}_{\rm fg} = \sum_{i=1}^{C-1} \frac{D_{i,C}}{D_C} \boldsymbol{\alpha}_i(\boldsymbol{\theta}_i), \tag{5}$$

$$\boldsymbol{\alpha}_{\rm los} = \sum_{i=1, i\neq C}^{N} \frac{D_{i,S}}{D_S} \boldsymbol{\alpha}_i(\boldsymbol{\theta}_i), \tag{6}$$

where C denotes the cluster plane, while S denotes the source plane.

2.2.2. Computing Each Plane

After rotating and restricting the simulation coordinates, we use two-dimensional binning to construct maps of surface mass density Σ_i. We find that maps with 1200^2 pixels offer a good balance between resolution and particle statistics (i.e., avoiding shot noise that would arise with small bins). Figure 3 shows sample density maps for three redshifts.

For lensing calculations, the surface mass density is scaled by the critical density for lensing to obtain the convergence:[2]

$$\kappa_i = \frac{\Sigma_i}{\Sigma_{{\rm crit},i}} \quad \text{where} \quad \Sigma_{{\rm crit},i} = \frac{c^2}{4\pi G D_i}. \tag{7}$$

(Here i still denotes the index of the plane.) The lens potential ψ for each plane can then be found from the Poisson equation,

$$\nabla^2 \psi(\boldsymbol{\theta}) = 2\kappa(\boldsymbol{\theta}). \tag{8}$$

We solve this equation for each plane using Fourier transforms. Let $\boldsymbol{k}$ be the wavevector, and $\hat{\psi}(\boldsymbol{k})$ and $\hat{\kappa}(\boldsymbol{k})$ be the lens potential and convergence in Fourier space. Then, Equation (8) transforms to

$$\hat{\psi} = -\frac{\hat{\kappa}}{2\pi^2 |\boldsymbol{k}|^2}. \tag{9}$$

---

[2] Here the critical density is computed for a source at infinity because the source distance is explicitly folded into the lens equation rather than factored into the convergence.

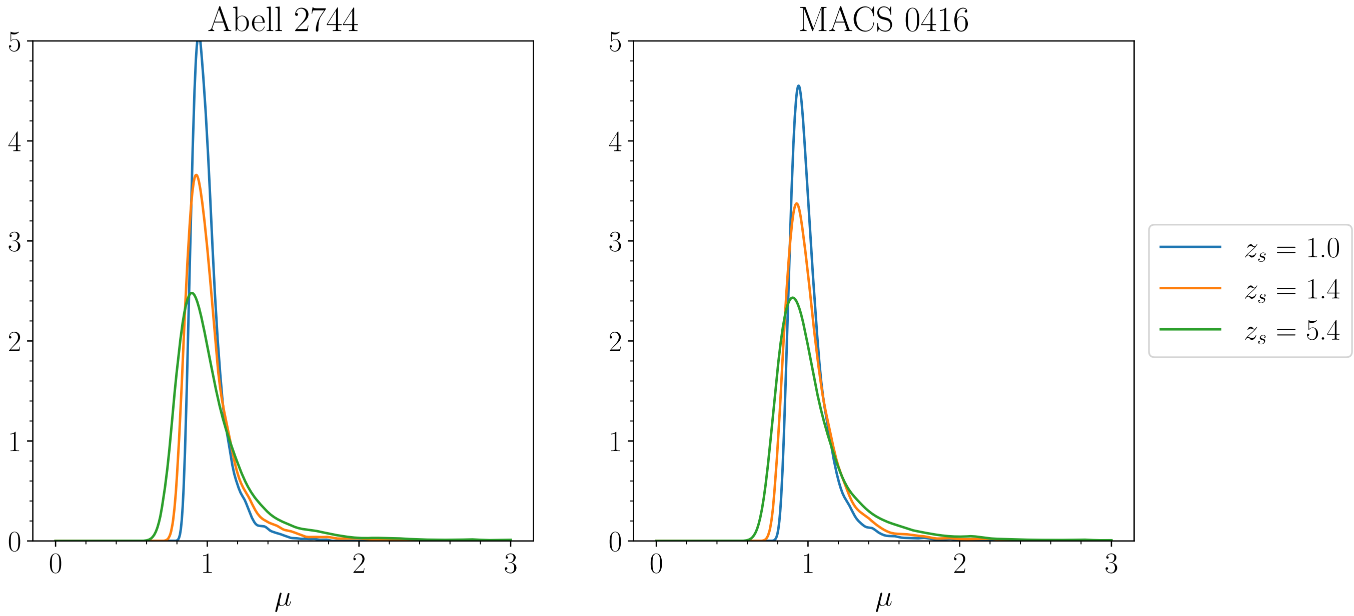

Figure 7. Distributions of cosmic magnification for the three sample source redshifts. As in Figure 6, the curves are computed from the samples using Gaussian KDE curves for magnification at three source redshifts. To remove outliers, we omit the 1% extremes before determining the domain plotted here.

Table 1
Statistics and Fit Parameters for Shear and Convergence

	z_s	Mean	St. Dev.	Shape (s)	Loc.	Scale
$\gamma_{c,s}$	1.0	0.000	0.041	⋯	0.000	0.041
	1.4	−0.001	0.078	⋯	−0.001	0.077
	5.4	−0.001	0.081	⋯	−0.001	0.081
$1+\kappa$	1.0	0.999	0.057	0.429	0.879	0.110
	1.4	0.999	0.109	0.394	0.740	0.239
	5.4	1.000	0.113	0.393	0.731	0.249

Note. Columns (3)–(4) give the mean and standard deviation for the shear and convergence distributions computed with the A2744 image configuration for the same redshifts shown in Figure 6 (results are also available for other redshifts). Columns (5)–(7) give parameters for normal (for shear) and log-normal (for convergence) fits to the distributions. The γ_c and γ_s distributions have similar statistics, and hence have been grouped together. The fits are done in `Python` using the `scipy.stats` package, and the full distributions can be reconstructed using that package.

Numerically, since $\boldsymbol{k}^2 = 0$ at the origin, we regularize by setting $\hat{\psi}(\mathbf{0}) \equiv 0$. This is equivalent to setting the mean convergence to zero, so to compensate, we take the potential obtained from the Fourier analysis and add a term that corresponds to a mass sheet whose density is the average convergence, $\bar{\kappa}$, of the original density map. In other words, the final lens potential is

$$\psi = \psi_{\mathrm{FT}} + \frac{1}{2}\bar{\kappa}|\boldsymbol{\theta}|^2. \tag{10}$$

Finally, the deflection is the gradient of the lens potential: $\boldsymbol{\alpha} = \nabla\psi$.

2.2.3. Characterizing Deflections

We compute LOS deflections at a set of observed image positions $\boldsymbol{\theta}_\nu$, where ν is an index that runs over the images. Any deflection that is constant across the images is unobservable (it merely translates the source plane), so we are actually interested in differential deflections. For a given set of images, we define a reference point at the center of the image configuration and assume it has a source redshift $z_s = 2.0$. The deflection of this "dummy" image is subtracted from the deflection of each image in the set to obtain differential deflections.

Consider the deflection for an image at position $\boldsymbol{\theta} = (x, y)$. It is worthwhile to decompose this deflection into contributions from an effective convergence (κ) and shear (γ_c and γ_s), and contributions from higher-order terms ($\delta\boldsymbol{\alpha}$):

$$\begin{aligned} \alpha_{\mathrm{sim},x} &= \frac{D_{LS}}{D_S}[a_x + (\kappa + \gamma_c)x + \gamma_s y] + \delta\boldsymbol{\alpha}_x \\ \alpha_{\mathrm{sim},y} &= \frac{D_{LS}}{D_S}[a_y + \gamma_s x + (\kappa - \gamma_c)y] + \delta\boldsymbol{\alpha}_y. \end{aligned} \tag{11}$$

This is useful because shear is often included as a free parameter in lens modeling; if we can measure the distribution of LOS shear from our analysis, we can use it as a prior or constraint on future lens models. Convergence is typically omitted from lens models because of the mass sheet degeneracy (e.g., M. V. Gorenstein et al. 1988; P. Saha 2000); but if we can constrain its distribution then it could be included in future models (this type of analysis has been done for galaxy-scale lenses; see, e.g., S. H. Suyu et al. 2010; Z. S. Greene et al. 2013; C. E. Rusu et al. 2017; P. Wells et al. 2023). Higher-order terms in the deflection distribution are typically omitted as well, especially for cluster lenses, because they have not been known, but we now have the opportunity to determine them directly.

We can find the values of $\boldsymbol{p} \equiv (\kappa, \gamma_c, \gamma_s, a_x, a_y)$ in Equation (11) as follows. Define a matrix

$$\boldsymbol{M}_\nu = \frac{D_{L\nu}}{D_\nu}\begin{bmatrix} x_\nu & x_\nu & y_\nu & 1 & 0 \\ y_\nu & -y_\nu & x_\nu & 0 & 1 \end{bmatrix} \tag{12}$$

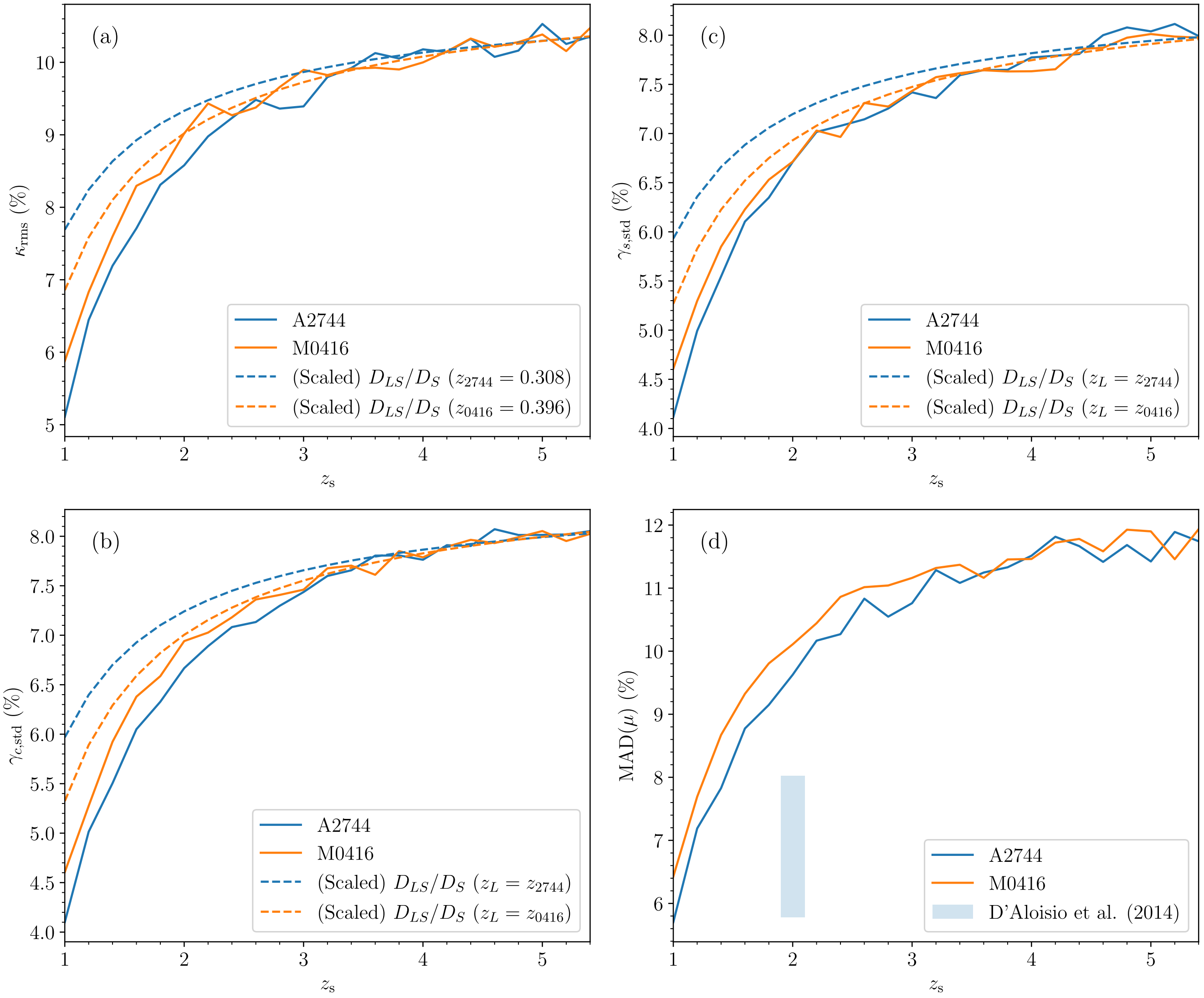

Figure 8. rms values of κ (panel a), γ_c (b), and γ_s (c) as a function of source redshift for the two cluster image configurations. The dashed curves show the geometric factor D_{LS}/D_S for each cluster redshift, scaled to match the simulation curves at high source redshift. As discussed in the main text, the fact that the simulation curves are steeper than the geometric curves indicates that convergence and shear have contributions from the entire line of sight. Panel (d) shows the median absolute deviation (MAD) instead of rms for magnification, to better handle extreme values; here, the shaded region depicts results from A. D'Aloisio et al. (2014).

for image ν, where a subscript ν on a distance reminds us to use the source redshift appropriate for image ν. Then, the deflection caused by convergence and shear would have the form $\boldsymbol{M}_\nu \boldsymbol{p}$. We can find the optimal values for $\boldsymbol{p}$ by minimizing

$$\chi^2 = \sum_\nu |\boldsymbol{M}_\nu \boldsymbol{p} - \boldsymbol{\alpha}_{\mathrm{sim},\nu}|^2. \tag{13}$$

Solving $\partial\chi^2/\partial\boldsymbol{p} = 0$ yields

$$\left(\sum_\nu \boldsymbol{M}_\nu^\top \boldsymbol{M}_\nu\right)\boldsymbol{p} = \sum_\nu \boldsymbol{M}^\top \boldsymbol{\alpha}_{\mathrm{sim},\nu}. \tag{14}$$

Once we solve this linear equation to find the convergence and shear for this set of deflections, we can compute the higher-order terms as

$$\delta\boldsymbol{\alpha}_\nu = \boldsymbol{\alpha}_{\mathrm{sim},\nu} - \boldsymbol{M}_\nu \boldsymbol{p} - \boldsymbol{\alpha}_0, \tag{15}$$

where $\boldsymbol{\alpha}_0$ is the deflection of the dummy image.

Finally, we compute the rms deflection from higher-order terms,

$$\delta\alpha_{\mathrm{rms}} = \sqrt{\frac{1}{N_{\mathrm{img}}}\sum_\nu |\delta\boldsymbol{\alpha}_\nu|^2}\,. \tag{16}$$

This is useful as a simple way to assess whether the LOS has a significant effect on lensing.

2.2.4. Deflection Statistics

In the lens modeling framework of C. A. Raney et al. (2021), the LOS and foreground deflections are treated as random variables and marginalized in a Bayesian analysis. Consider a vector $\boldsymbol{\delta}$ that contains the x- and y-components of LOS deflection computed at all of the observed image positions: $\boldsymbol{\delta} = (\delta\alpha_{1x}, \delta\alpha_{1y}, \delta\alpha_{2x}, \delta\alpha_{2y}, \ldots)$. We focus on the higher-order terms since the convergence and shear can be handled explicitly in the lens model. We can construct $\boldsymbol{\delta}$ for both the LOS and foreground components of deflection. Then, for the Bayesian lens modeling analysis, the quantities we need to

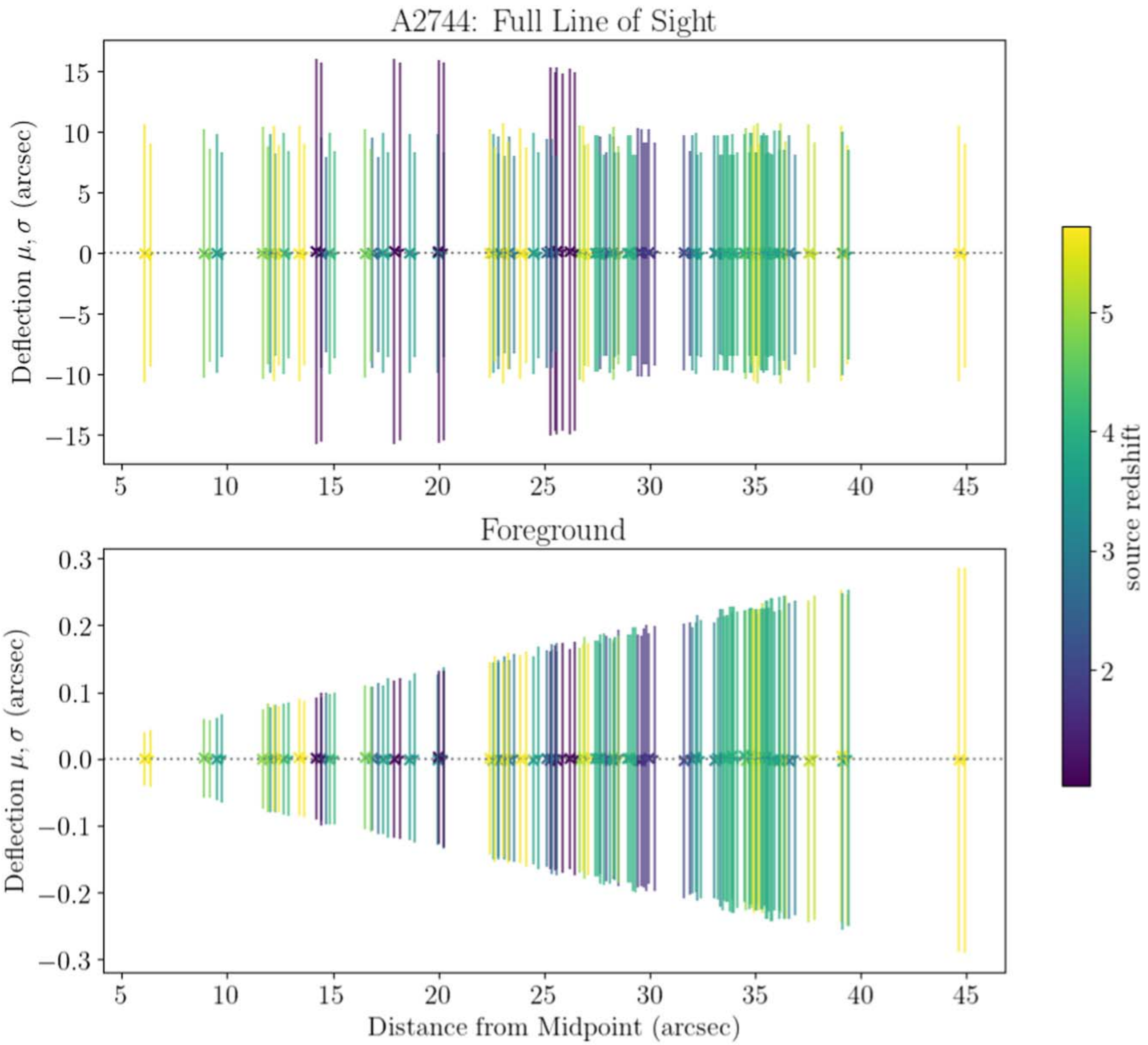

Figure 9. Deflections from higher-order terms, computed for the A2744 image configuration. We show the mean (points) and standard deviation (error bars) for each image, as a function of the distance of the image from the midpoint of the image configuration; the x- and y-components of deflection are slightly offset horizontally for clarity. The color indicates source redshift. The top panel shows the full LOS deflection $\delta\boldsymbol{\alpha}_{\rm los}$; note that convergence and shear effects have been separated out here. The bottom panel shows the foreground deflection $\boldsymbol{\alpha}_{\rm fg}$; here, convergence and shear effects have not been removed because foreground convergence and shear are not explicitly handled in most lens models.

compute are the mean vector $\langle \boldsymbol{\delta} \rangle$ and the covariance matrix $\mathbf{C}_\delta$. See Equations (A12)–(A14) in Appendix A of C. A. Raney et al. (2021) for details about how these quantities are used. Note that we need to compute not only the covariance among LOS quantities but also the cross-covariance between LOS and foreground quantities since the foreground portion of each LOS contributes to both.

2.3. Cluster Fields

To obtain specific image configurations for computing deflection statistics, we consider two of the HFF clusters. (i) MACS J0416−1.2023 (M0416) is part of the Massive Cluster Survey (MACS) and located at redshift $z = 0.396$ (H. Ebeling et al. 2001). (ii) A2744 is part of the Abell cluster catalog and located at redshift $z = 0.308$ (G. O. Abell et al. 1989). In both cases, we use the same sets of images that were studied by C. A. Raney et al. (2020a): M0416 has 95 images of 35 sources, while A2744 has 71 images of 24 sources. The image configurations are shown in Figure 4.

3. Results and Discussion

We now present the results of our analysis. For each image configuration, we sample the distribution by generating 10,000 random realizations. For each one, we apply random shifts to all of the lens planes to generate a new total deflection map. We also randomly rotate and translate the image configuration, as shown in Figure 5. We compute the set of deflections $\boldsymbol{\alpha}_{{\rm sim},\nu}$ and then decompose them into convergence, shear, and higher-order terms as described in Section 2.2.3. We separately analyze the convergence/shear and higher-order terms.

As a reminder, our main results use the full IllustrisTNG simulation, which includes stars and gas as well as dark matter.

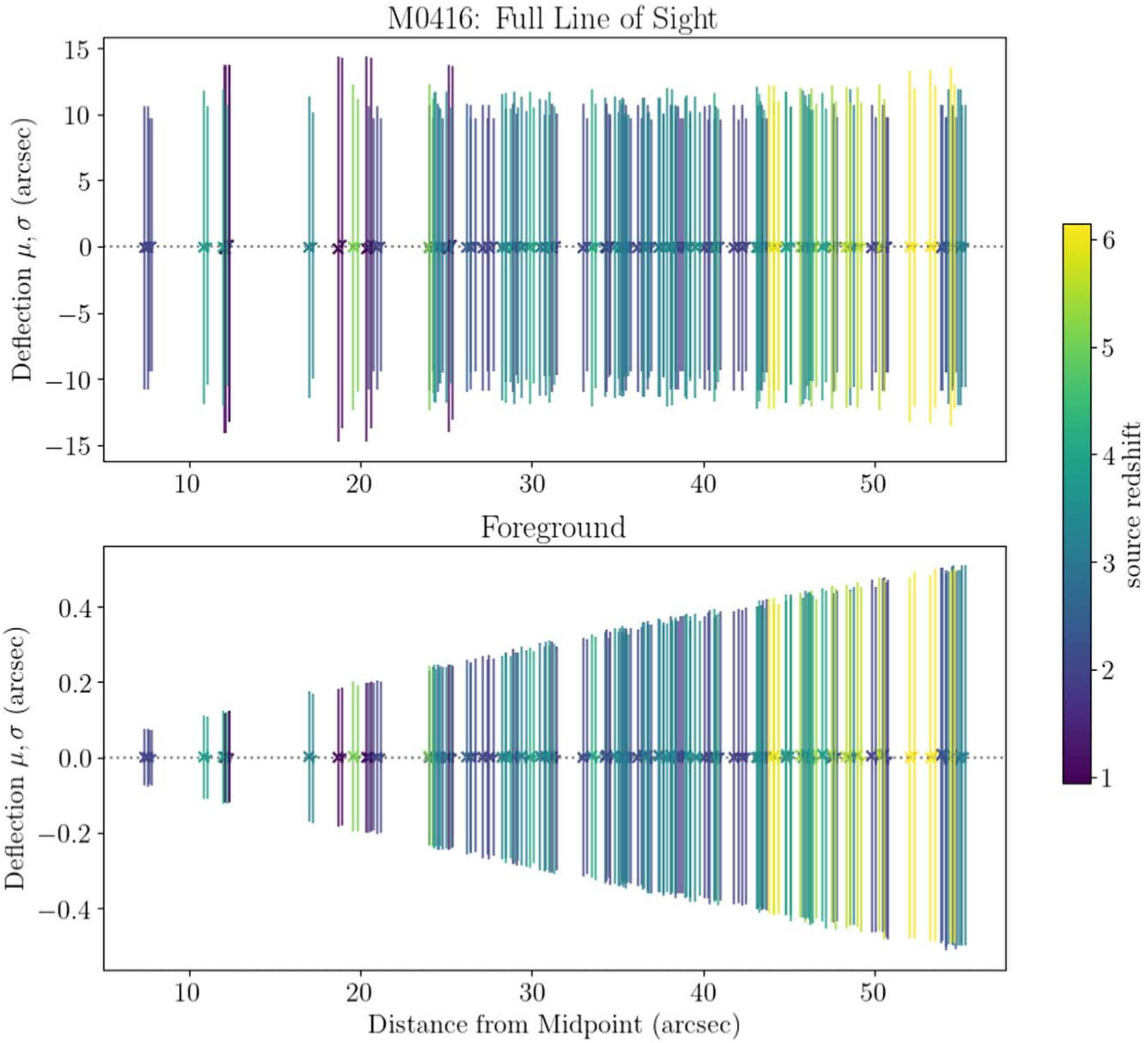

Figure 10. Similar to Figure 9, but for the M0416 image configuration.

For comparison, we also present results for a dark-matter-only simulation in the Appendix. The two simulations give very similar results, which makes sense because the distribution of matter on large scales is not especially sensitive to baryonic effects.

3.1. Convergence and Shear

We begin with cosmic convergence and shear to connect with previous work and provide information that can be used as constraints or priors on future lens models. For this analysis, we override the actual redshifts of the sources and assume that all of the images have the same source redshift;[3] we can then explore how the convergence and shear vary with z_s. For each assumed source redshift, we process the simulation deflections to determine the convergence κ and the two components of shear γ_c and γ_s.

Figure 6 shows the convergence and shear distributions for both image configurations for three representative source redshifts: $z_s = 1$, 1.4, and 5.4 were chosen to illustrate the evolution of the distributions.[4] The shear distributions are approximately symmetric and centered on zero, which makes sense because there is no preferred direction in the Universe. The convergence distributions are skewed; they tend to peak slightly below zero because most locations in the Universe are slightly underdense, and have a tail to positive values because nonlinear structure formation can create large overdensities. Overall, as the source redshift increases the distributions broaden, and the peak of the convergence distribution becomes slightly more negative. Results for the two cluster fields differ slightly because of the different cluster redshifts.

---

[3] In the observed lens systems, the source redshift is closely tied to the image configuration, so any modeling analysis cannot override the true redshifts. Our analysis does not involve any lens modeling though (as it does not attempt to include the cluster itself). We simply use the observed images to obtain a realistic set of image positions.

[4] For each redshift, we have 10,000 realizations of (κ, γ_c, γ_s). We use Gaussian kernel density estimation to compute smooth distributions from the samples.

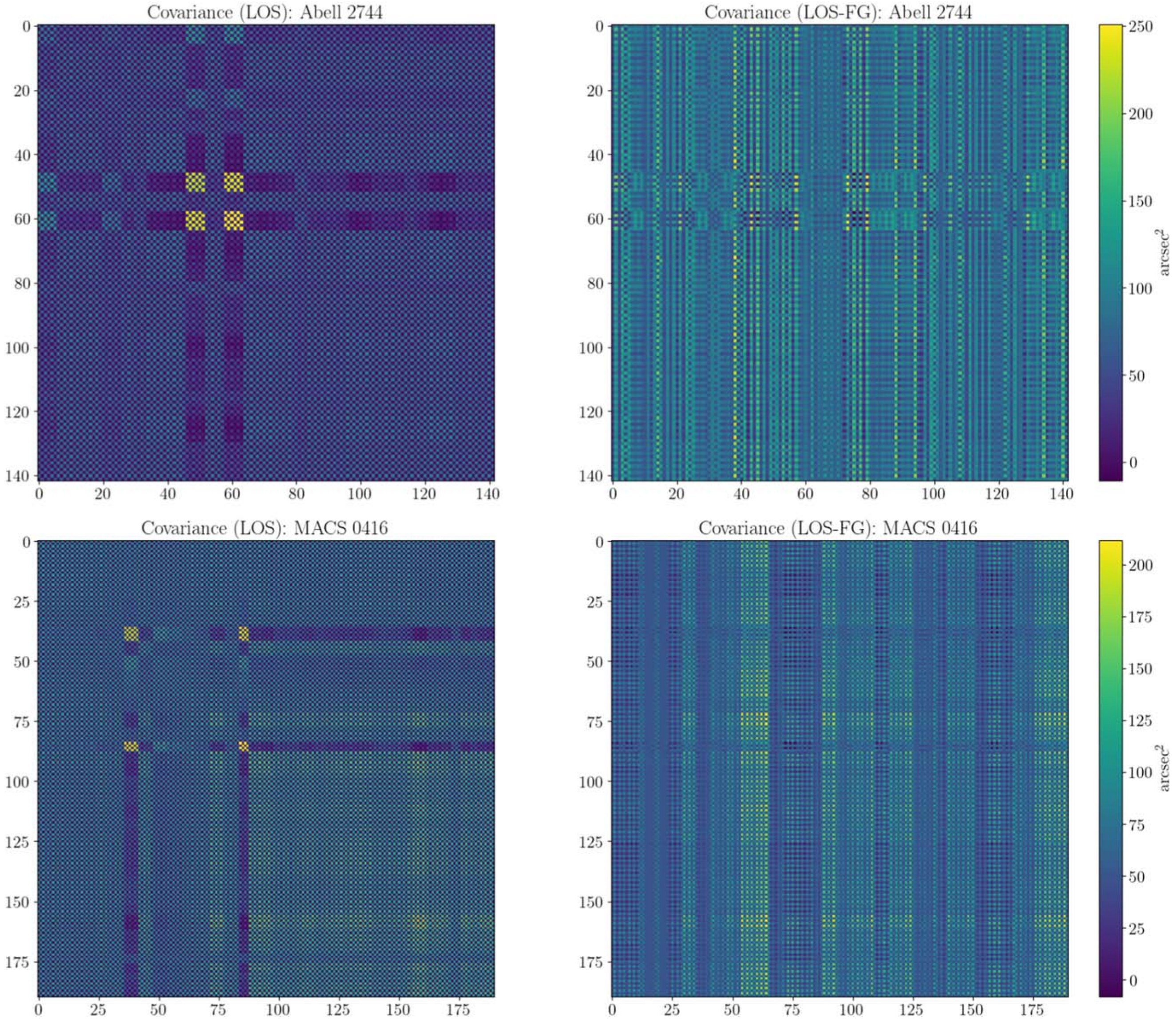
Covariance (LOS): Abell 2744

Covariance (LOS-FG): Abell 2744

Covariance (LOS): MACS 0416

Covariance (LOS-FG): MACS 0416

Figure 11. Deflection covariance matrices for the A2744 (top) and M0416 (bottom) image configurations. The left images show the covariance matrices for the full line of sight; the right images show the covariance between the foreground component and the full LOS. The matrix indices loop over the x- and y-components of images ($1x$, $1y$, $2x$, $2y$,…). We use the same image indices as C. A. Raney et al. (2020a).

We find that the shear distributions are well-described by a normal distribution, while the $(1 + \kappa)$ distributions are well-described by a log-normal distribution. (The bottom row of Figure 6 compares the simulation samples shown by histograms with the normal and log-normal fits.) The parameters of the fitted distributions are given in Table 1.

Given the convergence and shear, we can compute the cosmic magnification as

$$\mu = \frac{1}{(1 - \kappa)^2 - \gamma_c^2 - \gamma_s^2}. \tag{17}$$

Figure 7 shows the magnification distributions. Because magnification is nonlinear and can formally diverge, the simulation results have a small number of significant outliers; we remove the extreme 1% data points (0.5% low and 0.5% high) when determining the domain for plotting the distributions. Like the convergence distributions, the magnification distributions are skewed with peaks slightly below 1 and tails to the right.

R. Bar-Kana (1996) and A. D'Aloisio et al. (2014) presented similar analyses of cosmic convergence and shear using their theoretical analyses based on the matter power spectrum. They reported rms values as a function of source redshift (see Figures 8 and 4 in the respective papers), so we show equivalent quantities in Figure 8. Because of outliers, for the magnification distribution, we instead use the median absolute deviation (MAD), which is a more robust statistic. In general, our values are somewhat larger than the previous results: for convergence, R. Bar-Kana reported $\kappa_{\rm rms}(z_s \sim 5) \sim 8\%$ compared to our $\sim 10\%$; and for magnification, A. D'Aloisio et al. reported $\mu_{\rm mad}(z_s \sim 2) \sim 6\%$–$8\%$ compared to our $9\%-10\%$.[5] These differences are reasonable given that the analyses used different cosmological parameters and methodologies.

---

[5] Note that A. D'Aloisio et al. (2014) actually reported a standard deviation. We converted their value to MAD assuming a normal distribution, but that conversion is model-dependent.

If the deflections were entirely due to convergence and shear in the cluster lens plane, the evolution with source redshift would be governed by the geometric factor D_{LS}/D_S, which is shown with the dashed curves in Figure 8. The simulation curves are steeper than the D_{LS}/D_S curve because of contributions from the entire LOS. There is some difference between the two fields because of the difference in the cluster redshift.

3.2. Higher-order Terms

To study deflection from higher-order terms, we rerun the calculations using the actual redshift for each source. Figures 9 and 10 show the results for the A2744 and M0416 image configurations, respectively.

The mean deflections are close to zero, which makes sense because there is no preferred direction in the Universe. For A2744, the average over all images is $-0\rlap{.}''06$ for the full LOS and has a magnitude less than $0\rlap{.}''001$ for the foreground. For M0416, the corresponding values are $0\rlap{.}''009$ for the full LOS and less than $0\rlap{.}''001$ for the foreground.

The LOS deflection distributions are quite broad, however. For A2744, the standard deviation averaged over all images is $9\rlap{.}''8$, while the rms deflection is $14\rlap{.}''1$. For M0416, the average standard deviation is $11\rlap{.}''0$ and the rms is $15\rlap{.}''6$. These values are considerably larger than the residuals for HFF lens models, which are typically below $1''$. Thus, our results indicate that the effects of LOS deflection are not negligible and need to be taken into account in future lens models. There are likely to be strong covariances among the deflections for different images, so it is important to compute the covariance matrices as shown in Figure 11. The lens modeling framework introduced by C. A. Raney et al. (2021) provides a way to generate new lens models that account for LOS effects through the mean vector (which we have found to be equivalent to zero) and the covariance matrices.

By contrast, the foreground deflection distributions are considerably smaller, thanks to smaller path lengths and weaker geometric effects compared with the full LOS.

4. Conclusions

To summarize, we have analyzed contributions from cosmological large-scale structure to systematic uncertainties in cluster lens models. Specifically, we have used ray tracing through the `TNG100-3` cosmological simulation to compute the distribution of deflections by large-scale structure, using the HFF lensing clusters A2744 and MACS 0416 as examples.

We find that the cosmic shear distribution is Gaussian in each component, with a standard deviation of 4%–8% depending on the redshift of the source. The cosmic convergence distribution is skewed such that $1+\kappa$ is consistent with a log-normal distribution; the standard deviation of κ is at the level of 6%–11%, although it is better to use the parameters in Table 1 to capture the shape of the distribution. The redshift dependence of shear and convergence cannot be explained by the geometric factor D_{LS}/D_S that would arise if all of the contributions were from a single plane at the lens redshift. Our results for cosmic shear, convergence, and magnification are broadly consistent with previous theoretical studies using power-spectrum models (R. Bar-Kana 1996; O. Host 2012; A. D'Aloisio et al. 2014).

There are contributions to deflection beyond convergence and shear because of nonlinearities in structure formation and lensing. For these higher-order terms, mean deflections are effectively zero because there is no preferred direction in the Universe, but the scatter is significant. The rms deflection from higher-order terms is $14\rlap{.}''1$ for A2744 and $15\rlap{.}''6$ for M0416. These values are significantly higher than the residuals between observational data and older lens models ($\lesssim 1''$). The rms deflection is a bit of a blunt instrument because the deflections for different images are likely to have significant covariances, so we have computed full covariance matrices as well.

We conclude that deflection from large-scale structure is not negligible for cluster lensing. Future lens models can use our results for cosmic shear and convergence as constraints or priors on those model parameters. They can also incorporate the statistics of higher-order terms by using covariance matrices like the ones we have computed in the theoretical framework presented by C. A. Raney et al. (2021). It will be interesting to see how much large-scale structure contributes to the overall error budget for cluster lens models, and whether it resolves differences between results from different HFF lens modeling teams.

Acknowledgments

We thank the HFF program for making high-quality gravitational lensing data accessible. We also thank Lana Eid, Somayeh Khakpash, Io Kovach, and Dilys Ruan for helpful conversations and comments on the manuscript. We thank the anonymous referee for helpful comments on the manuscript. This project began as part of the Aresty Summer Science Program offered by the Aresty Research Center at Rutgers University–New Brunswick. We acknowledge support from the US National Science Foundation through grant AST-1909217.

Data Availability

`TNG100-3` simulation snapshots are publicly available on the `IllustrisTNG` Project: https://www.tng-project.org. All other data and code are publicly available at https://github.com/aniruddhamadhava/RU_Lensing_Data.

Appendix

It is interesting to consider whether our results are sensitive to baryonic effects by repeating the analysis using a dark-matter-only version of the Illustris TNG simulation. Specifically, we apply the same methodology to data from the `TNG100-3-Dark` simulation. This simulation has the same number of dark matter particles as `TNG100-3`, but the particle mass is about 19% higher to account for the absence of baryons and ensure that the simulation has the intended mean density.

Overall, we find that results from the dark-matter-only simulation are very similar to the results from the full simulation. For example, Figure 12 compares the convergence and shear distributions for the two cases using the A2744 image configuration, and Table 2 summarizes properties of the convergence and distributions (for comparison with Table 1). Seeing similar results makes sense because dark matter is more abundant at cosmic scales, and hence plays a bigger role in cosmological large-scale structures than baryons.

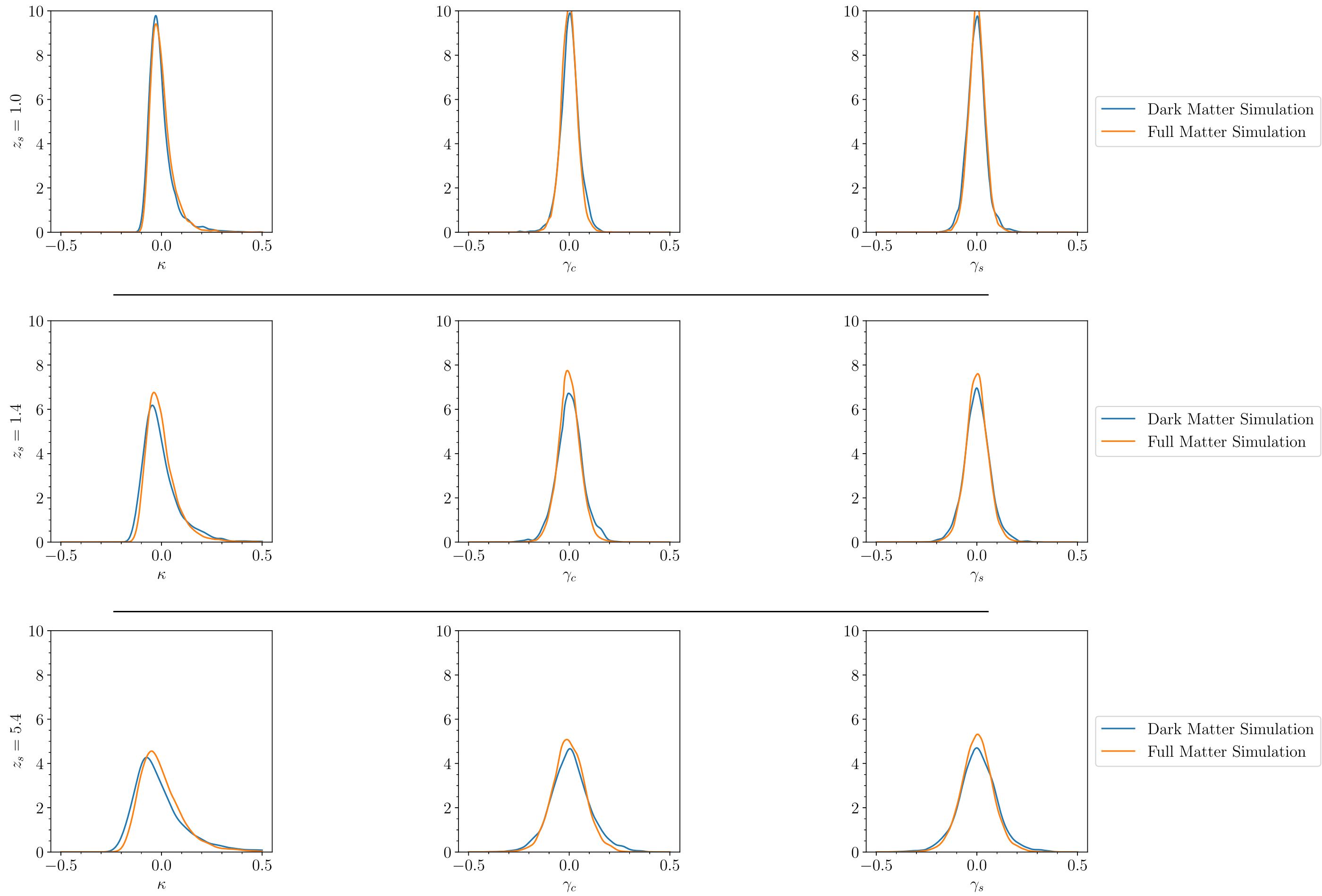

Figure 12. Comparison of the convergence (κ) and shear ($\gamma_{c,s}$) distributions for the full- and dark-matter analyses using the A2744 image configuration. As in Section 3, we illustrate the results for $z_s = 1$, 1.4, 5.4. The distributions for the two analyses are fairly consistent with each other. We provide key statistics, like the mean and standard deviation, in Table 2.

Figures 13 and 14 show the deflection analysis for the A2744 and M0416 image configurations, respectively (for comparison with Figures 9 and 10). As before, the mean deflections are approximately zero since there is no preferred direction in the Universe. For A2744, the standard deviation averaged over all images is $9\overset{''}{.}8$, while the rms is $14\overset{''}{.}1$. For M0416, the corresponding values are $10\overset{''}{.}8$ and $15\overset{''}{.}4$.

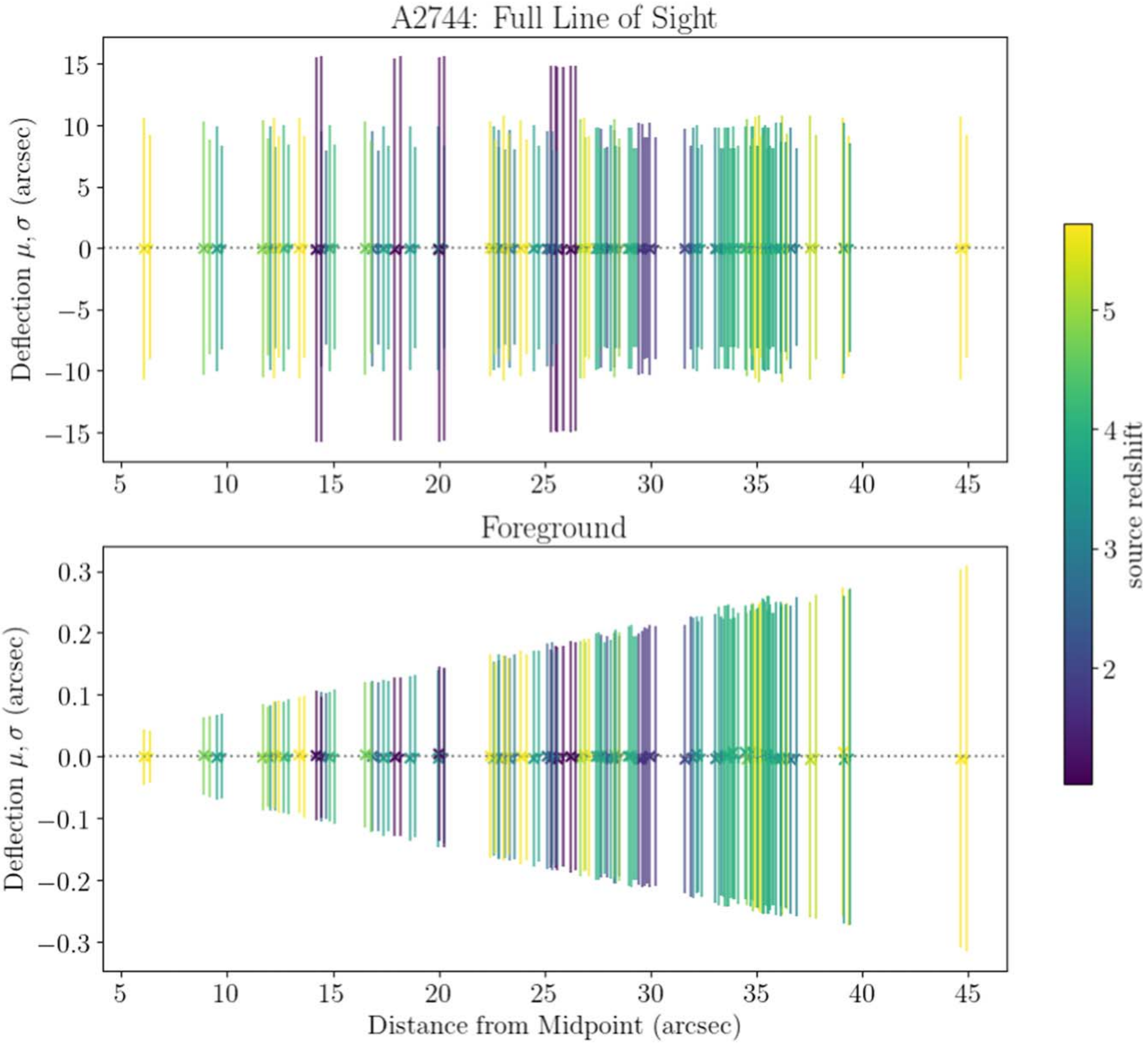

Figure 13. Similar to Figure 9, but for the dark-matter-only simulation.

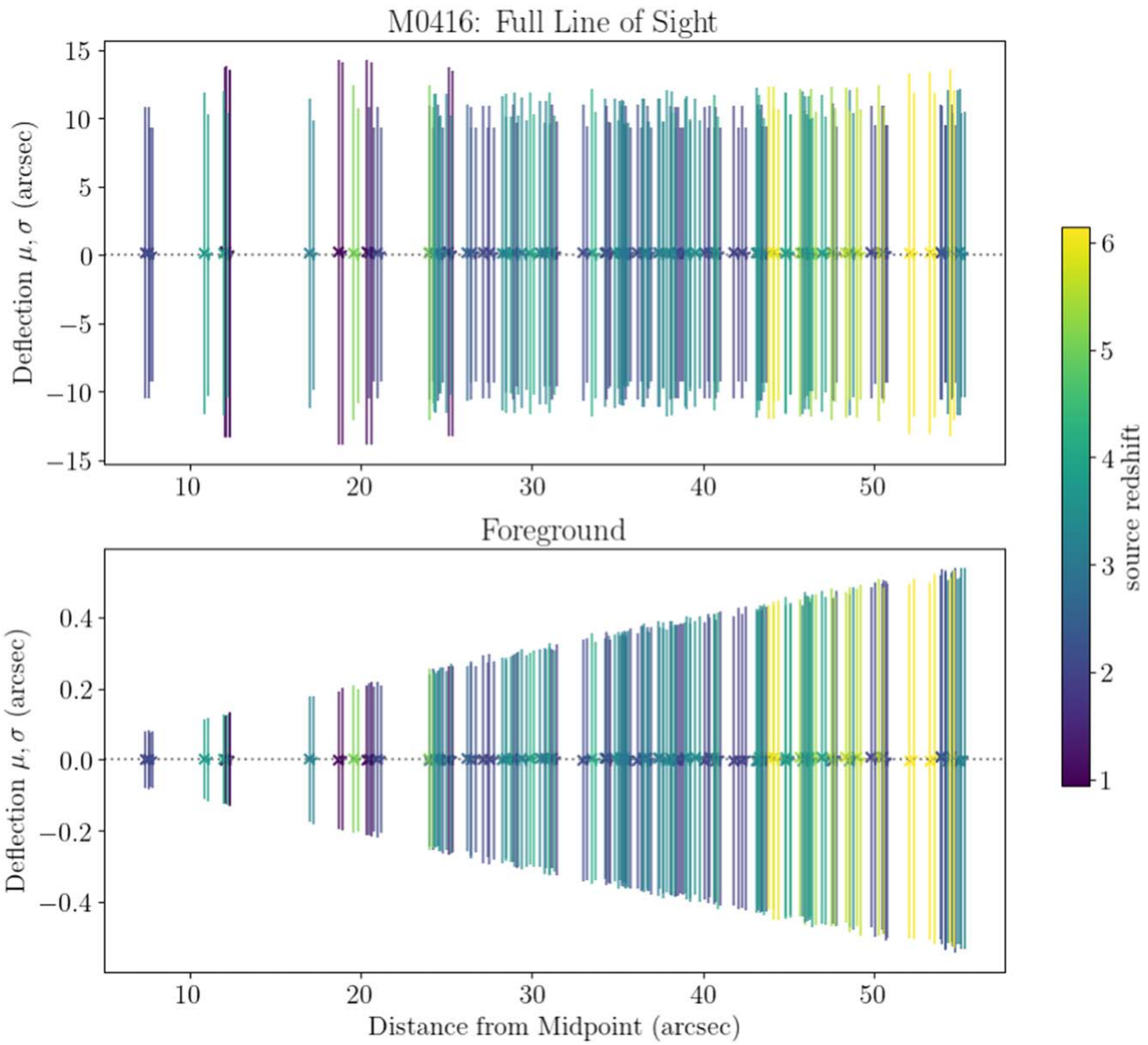

Figure 14. Similar to Figure 10, but for the dark-matter-only simulation.

Table 2
Statistics and Fit Parameters for Shear and Convergence: Dark Matter Only

	z_s	Mean	St. Dev.	Shape (s)	Loc.	Scale
$\gamma_{c,s}$	1.0	0.003	0.047	⋯	0.003	0.047
	1.4	0.003	0.065	⋯	0.003	0.065
	5.4	0.007	0.099	⋯	0.006	0.099
$1+\kappa$	1.0	0.996	0.064	0.483	0.881	0.102
	1.4	0.998	0.096	0.485	0.820	0.158
	5.4	0.995	0.141	0.469	0.725	0.241

Note. Similar to Table 1, but for the dark-matter-only simulation.

References

Abell, G. O., Corwin, H. G. J., & Olowin, R. P. 1989, ApJS, 70, 1
Bar-Kana, R. 1996, ApJ, 468, 17
D'Aloisio, A., Natarajan, P., & Shapiro, P. R. 2014, MNRAS, 445, 3581
Ebeling, H., Edge, A. C., & Henry, J. P. 2001, ApJ, 553, 668
Frye, B. L., Pascale, M., Foo, N., et al. 2023, ApJ, 952, 81
Furtak, L. J., Atek, H., Lehnert, M. D., Chevallard, J., & Charlot, S. 2021, MNRAS, 501, 1568
Gorenstein, M. V., Falco, E. E., & Shapiro, I. I. 1988, ApJ, 327, 693
Greene, Z. S., Suyu, S. H., Treu, T., et al. 2013, ApJ, 768, 39
Hilbert, S., Hartlap, J., White, S. D. M., & Schneider, P. 2009, A&A, 499, 31
Host, O. 2012, MNRAS, 420, L18
Kikuchihara, S., Ouchi, M., Ono, Y., et al. 2020, ApJ, 893, 60
Kneib, J.-P., & Natarajan, P. 2011, A&ARv, 19, 47
Lotz, J. M., Koekemoer, A., Coe, D., et al. 2017, ApJ, 837, 97
Marinacci, F., Vogelsberger, M., Pakmor, R., et al. 2018, MNRAS, 480, 5113
McCully, C., Keeton, C. R., Wong, K. C., & Zabludoff, A. I. 2014, MNRAS, 443, 3631
McCully, C., Keeton, C. R., Wong, K. C., & Zabludoff, A. I. 2017, ApJ, 836, 141
Naiman, J. P., Pillepich, A., Springel, V., et al. 2018, MNRAS, 477, 1206
Nelson, D., Pillepich, A., Springel, V., et al. 2018, MNRAS, 475, 624
Petters, A. O., Levine, H., & Wambsganss, J. 2001, Singularity Theory and Gravitational Lensing (Berlin: Springer)
Pillepich, A., Nelson, D., Hernquist, L., et al. 2018a, MNRAS, 475, 648
Pillepich, A., Springel, V., Nelson, D., et al. 2018b, MNRAS, 473, 4077
Planck Collaboration, Ade, P. A. R., Aghanim, N., et al. 2016, A&A, 594, A13
Raney, C. A., Keeton, C. R., & Brennan, S. 2020a, MNRAS, 492, 503

Raney, C. A., Keeton, C. R., Brennan, S., & Fan, H. 2020b, MNRAS, 494, 4771
Raney, C. A., Keeton, C. R., & Zimmerman, D. T. 2021, MNRAS, 508, 5587
Rusu, C. E., Fassnacht, C. D., Sluse, D., et al. 2017, MNRAS, 467, 4220
Saha, P. 2000, AJ, 120, 1654
Schneider, P., Ehlers, J., & Falco, E. E. 1992, Gravitational Lenses,
Springel, V., Pakmor, R., Pillepich, A., et al. 2018, MNRAS, 475, 676
Springel, V., White, S. D. M., Jenkins, A., et al. 2005, Natur, 435, 629
Suyu, S. H., Marshall, P. J., Auger, M. W., et al. 2010, ApJ, 711, 201
Weinberger, R., Springel, V., Hernquist, L., et al. 2017, MNRAS, 465, 3291
Wells, P., Fassnacht, C. D., & Rusu, C. E. 2023, A&A, 676, A95
Zimmerman, D. T., Keeton, C. R., & Raney, C. A. 2021, MNRAS, 508, 5602